An angular momentum integral equation for high-speed boundary layers

By A. Kianfar†, M. Di Renzo‡, C. Williams, A. Elnahhas AND P. L. Johnson†

The performance, efficiency, and durability of aerospace vehicles depends critically on the flow physics within thin boundary layers. Transitional and turbulent boundary layers significantly enhance both skin friction drag and surface heat flux, while potentially delaying separation. Recently, Elnahhas & Johnson (2022) introduced the angular momentum integral (AMI) equation to quantify how turbulence and other flow features throughout and above the boundary layer enhance or attenuate skin friction relative to an equivalent laminar boundary layer. This report extends the AMI equation to compressible flows. The compressible AMI equation is applied to direct numerical simulation data of turbulent boundary layers with a range of freestream Mach numbers and wall temperature boundary conditions. Using a novel shear-weighted average viscosity, the AMI results for compressible boundary layers up to Mach 7 show a striking similarity with the incompressible case when taken in reference to a self-similar laminar solution at the same Mach number and wall temperature. The main effect of compressibility on skin-friction coefficient is shown to be decreased ability of turbulence to transport momentum, $\overline{\rho}\widetilde{u_i''u_j''}$, due to lower near-wall mass densities. This investigation lays the groundwork for exploring the physics of enhanced surface heat flux through an analogous approach to the energy conservation equation.

1. Introduction

Transition to turbulence in boundary layers (BLs) is accompanied by a significant jump in skin friction and surface heat transfer. Depending on the application, this may be beneficial or deleterious. A fully turbulent wall-bounded flow is characterized by coherent structures with a wide range of length scales and differing wall-normal distances (Robinson 1991). The outer layer is populated by (very) large scale motions with streamwise extent (significantly) exceeding the boundary thickness (Smits *et al.* 2011). An approximately self-similar heirarchy of structures can be observed in the overlap (log-)layer (Marusic & Monty 2019). Nearer the wall in the buffer layer, the turbulent flow is organized by self-sustaining streamwise roll-streak patterns (Farrell & Ioannou 2012). Decades of research has compiled significant understanding of the structure of wall-bounded turbulence, but leveraging this knowledge base for effective modeling and flow control (e.g., drag reduction) at high Reynolds numbers remains challenging.

For fully developed flows such as channel or pipe flows, a second moment integral (or equivalently, a triple integration) of the mean momentum equation provides a simple method for quantifying the effect of Reynolds stresses on the friction factor compared to an equivalent laminar flow (Fukagata *et al.* 2002; Bannier*et al.* 2015). Interestingly, the

† University of California, Irvine
‡ Centre Européen de Recherche et de Formation Avancée en Calcul Scientifique, France

weighting of the Reynolds stress term in the resulting integral equation shows that turbulent fluctuations near the wall are more influential in the friction factor enhancement than those closer to the centerline. This so-called FIK relation has, for example, provided important guidance for flow control in the context of internal flows (Kim 2011). Recently, Elnahhas & Johnson (2022) developed the angular momentum integral (AMI) equation, which accomplishes for BLs what FIK equation does for internal flows (pipes, channels). Specifically, the AMI equation relates the skin-friction coefficient of any (turbulent) BL to the sum of an equivalent laminar skin-friction coefficient plus an (unweighted) integral of the Reynolds shear stress, along with other terms (e.g. freestream pressure gradients). In addition to the clear mathematical intepretation as enhancement or attenuation relative to an equivalent laminar BL, the AMI equation also has an intuitive physical interpretation in terms of torques that reshape the mean velocity profile, changing its angular momentum (moment-of-momentum) and affecting the slope at the wall.

The purpose of this report is to show the AMI equation for compressible ideal gas BLs and demonstrate it as an analysis tool for direct numerical simulation (DNS) results. The report is organized as follows. Section 2 derives the AMI equation for compressible BLs and provides an intuitive interpretation for each term related to the skin-friction coefficient. Then, Section 3 briefly summarizes the DNS results to be analyzed and the numerical method for generating laminar self-similar solutions. The AMI equation is applied to analyze DNS data for a range of freestream Mach numbers and wall temperature boundary conditions in Section 4. Conclusions are given in Section 5.

2. Background and theory

2.1. *Derivation of AMI for compressible flows*

The derivation of the AMI equation for compressible flows is outlined in this subsection. The density-weighted (Favre) averaged conservation of mass and streamwise momentum for a statistically steady 2D flow are, respectively,

$$\frac{\partial(\overline{\rho}\widetilde{u})}{\partial x} + \frac{\partial(\overline{\rho}\widetilde{v})}{\partial y} = 0 \quad \text{and} \tag{2.1}$$

$$\frac{\partial(\overline{\rho}\widetilde{u}^2)}{\partial x} + \frac{\partial(\overline{\rho}\widetilde{u}\widetilde{v})}{\partial y} = -\frac{\partial \overline{p}}{\partial x} + \frac{\partial}{\partial y}\left(\overline{\mu\frac{\partial u}{\partial y}} - \overline{\rho}\widetilde{u''v''}\right) + I_x^{\mathrm{M}}, \tag{2.2}$$

where the terms neglected by the BL approximations are gathered in I_x^{M}. Moreover, at the edge of the BL, the momentum equation yields

$$\rho_e U_e \frac{dU_e}{dx} = -\frac{dp_e}{dx}, \tag{2.3}$$

where the subscript $(\cdot)_{\mathrm{e}}$ stands for the edge variables or parameters. Subtracting Eq. (2.2) from Eq. (2.3), and adding U_e multiplied by Eq. (2.1), gives the x-momentum deficit equation

$$\frac{\partial[\overline{\rho}\widetilde{u}\,(U_e - \widetilde{u})]}{\partial x} + \frac{\partial[\overline{\rho}\widetilde{v}\,(U_e - \widetilde{u})]}{\partial y} + (\rho_e U_e - \overline{\rho}\widetilde{u})\,\frac{dU_e}{dx} = \frac{\partial}{\partial y}\left(\overline{\rho}\widetilde{u''v''} - \overline{\mu\frac{\partial u}{\partial y}}\right) - I_x^{\mathrm{M}}. \tag{2.4}$$

Integrating Eq. (2.4) across the BL, $\int_0^\infty [\cdot] dy$, neglecting I_x^{M}, yields the von Kármán momentum integral equation,

$$\frac{C_f}{2} = \frac{d\theta}{dx} + \frac{\theta}{U_e}\frac{dU_e}{dx}\left(2 + \frac{\delta^*}{\theta} + \frac{U_e}{\rho_e}\frac{d\rho_e}{dU_e}\right), \tag{2.5}$$

where the skin-friction coefficient, $C_f = 2\overline{\tau}_{\mathrm{w}}/\rho_e U_e^2$, is the non-dimensional mean wall shear stress, $\tau_{\mathrm{w}} = \mu_{\mathrm{w}}\left(\partial u/\partial y\right)_{\mathrm{w}}$. The compressible momentum and displacement thicknesses are, respectively,

$$\theta \equiv \int_0^\infty \frac{\overline{\rho}}{\rho_e}\frac{\widetilde{u}}{U_e}\left(1-\frac{\widetilde{u}}{U_e}\right)dy \quad \text{and} \quad \delta^* \equiv \int_0^\infty \left(1-\frac{\overline{\rho}}{\rho_e}\frac{\widetilde{u}}{U_e}\right)dy. \tag{2.6}$$

Eq. (2.5) is valid for both laminar and turbulent regimes; however, the contribution of turbulence is implicit. In other words, Eq. (2.5) does not directly quantify how turbulence impacts the skin-friction coefficient.

The AMI equation is derived by multiplying Eq. (2.4) by $(y-\ell(x))$ and integrating across the BL, $\int_0^\infty \{y-\ell(x)\}\,[\cdot]$. Applying the no-slip and no-penetration boundary conditions at the wall, the AMI relation reads

$$\begin{aligned}\frac{C_f}{2} &= \frac{1}{Re_\ell} + \frac{1}{\ell}\int_0^\infty \frac{-\bar{\rho}\widetilde{u''v''}}{\rho_e U_e^2}dy + \left\{\frac{d\theta_\ell}{dx} - \frac{\theta-\theta_\ell}{\ell}\frac{d\ell}{dx}\right\} + \frac{\theta_v}{\ell} + \frac{1}{\ell}\int_0^\infty \frac{\overline{(\mu-\mu_{\mathrm{ref}})\frac{\partial u}{\partial y}}}{\rho_e U_e^2}dy \\ &+ \left\{\frac{1}{U_e}\frac{dU_e}{dx}\left(\delta_\ell^* + 2\theta_\ell\right) + \frac{1}{\rho_e}\frac{d\rho_e}{dx}\theta_\ell\right\} + \mathcal{I}_{x,\ell}^{\mathrm{M}},\end{aligned} \tag{2.7}$$

where μ_{ref} is a reference viscosity to define the Reynolds number of a compressible BL, $Re_\ell = U_e\rho_e\ell/\mu_{\mathrm{ref}}$, and $\mathcal{I}_{x,\ell}^{\mathrm{M}}$ is generated by integration of I_x^{M}. The compressible momentum and displacement thicknesses introduced in Eq. (2.7) are, respectively,

$$\theta_\ell \equiv \int_0^\infty \left(1-\frac{y}{\ell}\right)\frac{\overline{\rho}}{\rho_e}\frac{\widetilde{u}}{U_e}\left(1-\frac{\widetilde{u}}{U_e}\right)dy \quad \text{and} \quad \delta_\ell^* \equiv \int_0^\infty \left(1-\frac{y}{\ell}\right)\left(1-\frac{\overline{\rho}}{\rho_e}\frac{\widetilde{u}}{U_e}\right)dy. \tag{2.8}$$

Finally, Eq. (2.7) also introduces the wall-normal momentum thickness,

$$\theta_v \equiv \int_0^\infty \frac{\overline{\rho}}{\rho_e}\frac{\widetilde{v}}{U_e}\left(1-\frac{\widetilde{u}}{U_e}\right)dy. \tag{2.9}$$

Following BL theory, the streamwise, x, direction may be interpreted as a time-like variable. In this perspective, Eq. (2.7) may be seen as an integral conservation principle for angular momentum about $\ell(x)$. As such, the terms in the AMI equation represent the sum of torques, equal to the growth of the BL's total angular momentum. Each term on the right side of Eq. (2.7) may be interpreted as follows:

(I) $\dfrac{1}{Re_\ell} \longrightarrow \dfrac{C_f}{2}$ of laminar zero-pressure-gradient BL at the same Re_ℓ,

(II) $\dfrac{1}{\ell}\displaystyle\int_0^\infty \frac{-\bar{\rho}\widetilde{u''v''}}{\rho_e U_e^2}dy \longrightarrow$ torque of turbulent momentum flux,

(III) $\dfrac{d\theta_\ell}{dx} - \dfrac{\theta-\theta_\ell}{\ell}\dfrac{d\ell}{dx} \longrightarrow$ streamwise growth of angular momentum thickness,

(IV) $\dfrac{\theta_v}{\ell} \longrightarrow$ torque due to mean wall-normal flux of momentum,

(V) $\dfrac{1}{\ell}\displaystyle\int_0^\infty \frac{\overline{(\mu-\mu_{\mathrm{ref}})\frac{\partial u}{\partial y}}}{\rho_e U_e^2}dy \longrightarrow$ effect of viscous deviation from μ_{ref}, zero if $\mu_{\mathrm{ref}} = \mu_2$,

(VI) $\dfrac{1}{U_e}\dfrac{dU_e}{dx}\left(\delta_\ell^* + 2\theta_\ell\right) + \dfrac{1}{\rho_e}\dfrac{d\rho_e}{dx}\theta_\ell \longrightarrow$ torque due to free-stream pressure gradient, and

(VII) $\mathcal{I}_{x,\ell}^{\mathrm{M}} \longrightarrow$ effects due to departure from BL assumptions.

2.2. *Reference viscosity and length scale for the AMI equation*

The skin-friction coefficient, C_f, the first and fifth terms of the right hand side of Eq. (2.7) originate from the first-order moment of viscous force (viscous torque) about $y = \ell(x)$

$$T_{\nu,\ell} = \int_a^\infty (y-\ell)\left[\frac{\partial}{\partial y}\left(\overline{\mu\frac{\partial u}{\partial y}}\right)\right] = \ell\tau_{\mathrm{w}} - \int_0^\infty \overline{(\mu-\mu_{\mathrm{ref}})\frac{\partial u}{\partial y}}dy - \mu_{\mathrm{ref}}U_e. \tag{2.10}$$

choosing the reference viscosity to be gradient-weighted viscosity defined as

$$\mu_{\mathrm{ref}} = \mu_2 = \frac{\int_0^\infty \overline{\mu\frac{\partial u}{\partial y}}dy}{\int_0^\infty \overline{\frac{\partial u}{\partial y}}dy} = \frac{1}{U_e}\int_0^\infty \overline{\mu\frac{\partial u}{\partial y}}dy, \tag{2.11}$$

makes the viscous deviation term (V) vanish by construction. With this,

$$T_{\nu,\ell} = \rho_e U_e^2 \ell\left(\frac{C_f}{2} - \frac{1}{Re_\ell}\right). \tag{2.12}$$

The length scale, ℓ, is set using a self-similar laminar BL solution with the choice of $T_{\nu,\ell} = 0$, thus $C_f/2 = 1/Re_\ell$. This choice enables the interpretation of the first right-hand side term of Eq. (2.7), $1/Re_\ell$, as the skin-friction coefficient of an equivalent laminar boundary condition. Note that the laminar BL solution may use incompressible (Blasius) or compressible equations, yielding different interpretations of the AMI equation (skin friction relative to which laminar BL?). In addition, the length scale may be chosen in different ways, for example, as $\ell \sim \theta$ or $\ell \sim \sqrt{x}$. These two choices also lead to different interpretations of the AMI equation, either as a comparison to a laminar BL at the same Re_θ or the same Re_x. For brevity, this report includes results with the choices $\mu_{\mathrm{ref}} = \mu_2$ and $\ell \sim \theta$ using the compressible flow laminar solution, $\ell = \ell_{2,C}$. In addition to removing the viscous deviation term from the AMI equation, the gradient-weighted viscosity (μ_2) is a physically motivated choice because it gives higher weight to the viscosity in regions of large velocity gradient, where the momentum flux is more sensitive to the value of μ. The choice of θ as the length scale is motivated by its physical relationship to the drag. Other choices of ℓ were explored for the incompressible case in Elnahhas & Johnson (2022).

3. Compressible turbulent BL data and numerical methods

This section discusses the compressible turbulent BL data used to evaluate the AMI relation, Eq. (2.7). The data are obtained from DNS of compressible BLs using turbulent recycling data with zero freestream pressure gradient (Di Renzo *et al.* 2020). In the numerical simulations, a sixth-order hybrid scheme, which uses a skew-symmetric formulation (Pirozzoli 2010) in smooth regions of the flow and a sixth-order targeted essentially non-oscillatory scheme across discontinuities (Fu *et al.* 2016), has been used for the spatial discretization of the Euler fluxes. Since the Reynolds number is relatively high for the simulations, a second-order central finite-difference stencil is applied for the diffusion fluxes. The time integration is conducted using the strong-stability-preserving third-order RungeKutta method (Gottlieb & Tadmor 2001). The system of equations for DNS is solved by the hypersonics task-based research (HTR) solver (Di Renzo *et al.* 2020).

The compressible fluid for the DNS is air considered as a perfect gas. The DNS data covers a range of edge Mach numbers, $0.6 \leq M_e \leq 7$, with different wall temperature

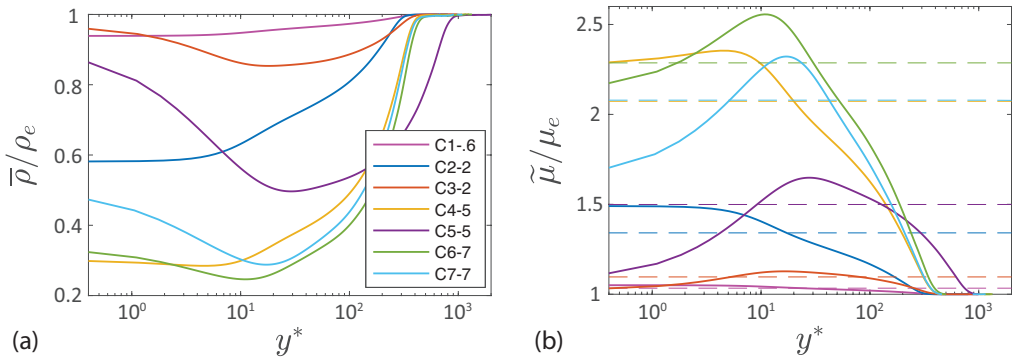

FIGURE 1. (a) Averaged normalized density, and (b) (Favre) averaged normalized viscosity; the dashed lines in panel (b) show the reference viscosity, $\mu_{\rm ref} = \mu_2$, for each case.

boundary conditions, such as cold walls, adiabatic walls, etc. Table 1 lists the edge and wall DNS inputs, the (normalized) reference viscosity for the AMI analysis, $\mu_{\rm ref} = \mu_2$; the minimum density within the BL; and the range of Reynolds number based on the reference viscosity, $Re_2 = \rho_e U_e \theta/\mu_2$.

The explicit effect of compressibility on momentum transport is due to the variation of density and viscosity within the BL, Eqs. (2.1) & (2.2). In Figure 1 (a,b) the profiles of the average density and (density-weighted) average viscosity, respectively, are presented with respect to the wall-normal direction normalized by the semi-local length scale, y^*. In all the simulations, the viscosity is computed as a function of temperature using Sutherland's law (with constants $T_0 = 273.15$ K and $S_0 = 110.4$ K) for air. The value of the chosen reference viscosity, μ_2, is also provided within the viscosity profile. Generally, higher M_e leads to lower density and higher viscosity. However, the wall temperature also has a crucial effect on both density and viscosity.

The mean velocity and Reynolds stress as a function of wall-normal distance are shown in Figure 2 (a,b), respectively. The mean velocity profiles in Figure 2(a) are normalized by U_e, reflecting their contributions to the integrands in the AMI equation. Figure 2 (b) confirms that the Reynolds stress profiles are similar near the wall when normalized by $\tau_{\rm w}$, as expected. The peak Reynolds stress does depend on the Reynolds number, which is not matched between each of the cases.

To obtain $\ell = \ell_{2,C}$ as a function of θ, such that $C_f/2 = 1/Re_\ell$ for ZPG compressible laminar BLs, the compressible self-similar equations under perfect gas assumptions must be solved. The system of self-similar ordinary differential equations is solved numerically by applying the second-order finite-difference scheme and a Newton-Raphson method with a line-search algorithm (Williams *et al.* 2021). The solver takes the edge flow parameters, provided in Table 1, and the wall temperature as inputs, and outputs the self-similar velocity and temperature profiles.

4. AMI analysis

This section examines the terms in the AMI equation, Eq. (2.7), using the DNS datasets summarized in Table 1. As discussed before, the choice of $\mu_{\rm ref} = \mu_2$ is used, so there is some physical reasoning for the choice of $\mu_{\rm ref}$ and the viscous deviation term is zero. Also, $\ell = \ell_{2,C}$ (based on momentum thickness) is chosen to isolate the skin-friction coefficient

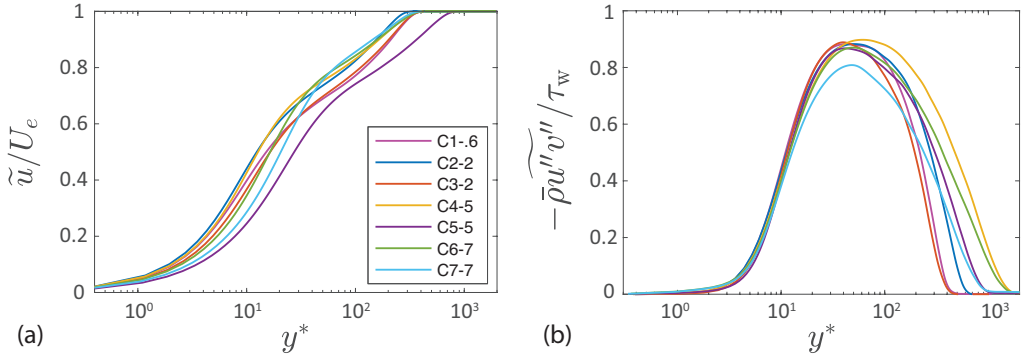

FIGURE 2. (a) Normalized mean velocity and (b) Reynolds shear stress normalized by the wall shear stress.

	Inputs				Outputs			
Case ID	M_e	$Re_{\delta_{in}}$	μ_w/μ_e	T_w/T_{aw}	ρ_w/ρ_e	ρ_{min}/ρ_e	μ_2/μ_e	Re_2
C1-.6	0.6	2800	1.05	1	0.94	0.94	1.03	294-959
C2-2	2	4736	1.49	1	0.58	0.58	1.34	299-928
C3-2	2	2800	1.02	0.6	0.96	0.85	1.09	244-816
C4-5	5	20000	2.27	0.6	0.3	0.28	2.07	446-1238
C5-5	5	10000	1.07	0.2	0.89	0.48	1.49	361-1104
C6-7	7	20000	2.12	0.3	0.33	0.24	2.27	314-901
C7-7	7	10000	1.63	0.2	0.49	0.28	2.07	182-571

TABLE 1. DNS inputs and some fundamental flow outputs; $Re_{\delta_{in}}$ is the Reynolds number based on the inflow BL thickness; Prandtl number $Pr = 0.72$, (non-dimensional) specific heat $c_p = 3.5$, and heat capacity ratio $\gamma = 1.4$ are set as constants and the same for all cases.

of a laminar BL at the same $Re_2 = \rho_e U_e \theta/\mu_2$ as the first term on the right hand side of Eq. (2.7), $1/Re_\ell$.

Figure 3 presents each term in the AMI equation. Data from an incompressible turbulent BL simulation (Wu et al. 2017) are also included. Figure 3(a) shows the $C_f/2$ (dashed line) and the summation of the right hand side of the AMI equation (solid line). The maximum (streamwise averaged) relative error of the right hand side is less than or (approximately) equal to 5% and depends mostly on the length of time used for averaging each simulation.

Figure 3(a,b) show that higher M_e generally leads to lower C_f in turbulent and laminar BLs, respectively. In addition to the trend with M_e, notice the influence of the wall temperature on C_f. Comparing C4-5 with C5-5 and C2-2 with C3-2 reveals that the skin-friction coefficient is smaller for lower wall density (at the same M_e). The density at the wall is inversely proportional to the wall temperature boundary condition, as the pressure is approximately constant across the boundary in these cases.

In Figure 3(c), the explicit effect of turbulent fluctuations on $C_f/2$ is shown. It is evident that the C_f trends shown in Figure 3(a) are matched by the trends for the Reynolds shear stress integral when using the compressible laminar solution as the baseline ($\ell = \ell_{2,C}$). This observation will be explored in more detail later in reference to Figure 4.

In Figure 3(d), the rate of streamwise growth of the angular momentum thickness is

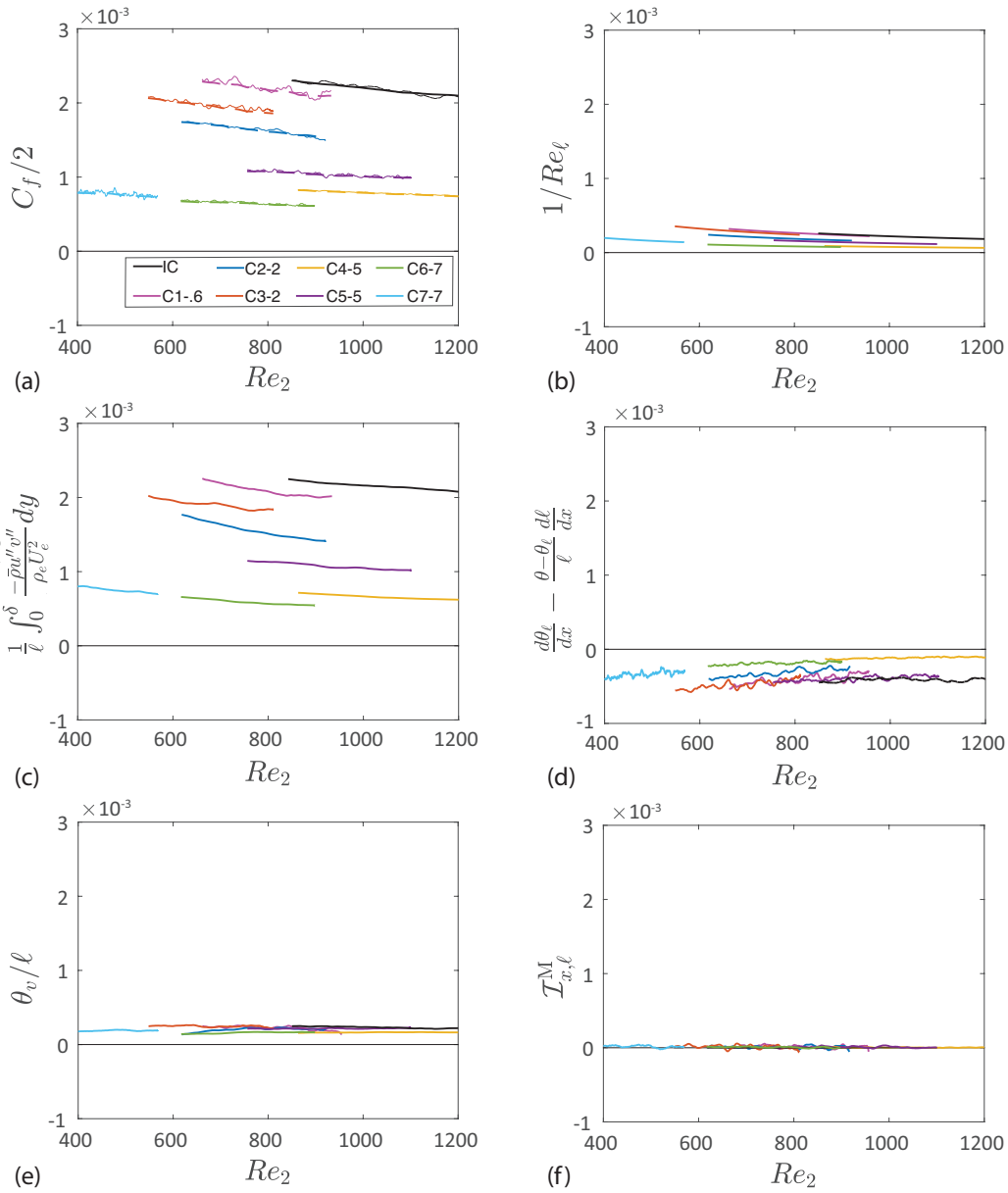

FIGURE 3. Budget of AMI based on $\ell = \ell_{2,C}$ and $\mu_{\mathrm{ref}} = \mu_2$ within the fully turbulent regime: (a) comparison between $C_f/2$ (dashed line) and the right hand side of the AMI equation (solid line), (b) laminar compressible contribution, (c) Reynolds shear stress direct contribution, (d) negative contribution of streamwise growth of BL thickness, (e) contribution of mean wall-normal flux, and (f) (negligible) contribution of terms ignored in the BL approximation. Black curves are for incompressible (IC) turbulent data.

shown for each case. This term has a negative contribution to the skin friction, as the turbulent BL grows thicker than its laminar counterpart, absorbing a small part of the Reynolds stress torque into the growth of the angular momentum. According to Figure

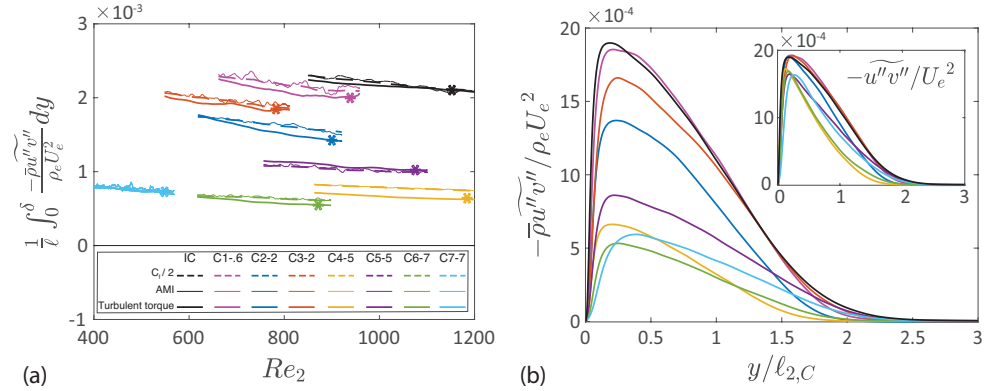

FIGURE 4. Turbulent torque in AMI budget: (a) contribution to $C_f/2$, (b) profile of integrand, $-\bar{\rho}\widetilde{u''v''}/\rho_e U_e^2$, and the inset shows profile of $-\widetilde{u''v''}/U_e^2$ (turbulent torque integrand without the density effect). "$*$" in (a) shows Re_2 at which (b) profiles are plotted.

3(d), the variation in this term is substantially less than that of the Reynolds shear stress integral in Figure 3(c). Nonetheless, a minor opposite trend can be observed.

The contribution of the mean wall-normal flux to C_f is presented in Figure 3(e). For a fully turbulent regime, this flow feature has a relatively weak influence and does not vary significantly with streamwise direction, consistent with previous observations of incompressible flows (Elnahhas & Johnson 2022; Kianfar *et al.* 2022). Its trend with respect to M_e and T_w is also weak. Figure 3(f) confirms that the terms typically neglected in BL theory are indeed small. There are two other terms not shown in Figure 3. First, the torque due to the freestream pressure gradient is also negligible because the simulations are run for a flat plate geometry with nominally zero pressure gradient. Second, the torque due to viscous deviation is zero by construction ($\mu_\mathrm{ref} = \mu_2$).

It is clear from Figure 3, particularly panels (a) and (c), that the skin friction trend with M_e and T_w can be explained mostly in terms of the Reynolds shear stress normalized by $\rho_e U_e^2$. Figure 4(a) compactly shows how the trend of the Reynolds shear stress integral closely matches that of $C_f/2$. A closer look at the Reynolds shear stress integrand is shown in Figure 4(b). The Reynolds shear stress is there normalized such that the integral under the curve corresponds to the value in Figure 4(a) at one particular streamwise location (indicated by the "*" symbol for each simulation). Normalized by $y/\ell_{2,C}$, the thickness of the turbulent layer in Figure 4(b) is roughly the same for each case. This observation underscores the relevance of the compressible laminar BL solution through the use of $\ell_{2,C}$. Use of the incompressible (Blasius) laminar solution does not lead to a similar effect (not shown). The peak value of the integrand, $-\bar{\rho}\widetilde{u''v''}/\rho_e U_e^2$, evidently determines the M_e and T_w trend observed in the Reynolds shear stress integral. The primary reason for this trend is the lower mean densities within higher M_e and higher T_w BLs. To demonstrate this, inset of Figure 4(b) removes the effect of $\overline{\rho}/\rho_e$ from the Reynolds shear stress integrand plot and a significant collapsing of the peak values is observed. Consequently, it follows that the primary effect of compressibility on the skin-friction coefficient in turbulent Bls is that lower mass density in the near-wall region, depicted in Figure 1(a), decreases the ability of correlated velocity fluctuations (i.e., the Reynolds shear stress) to transport momentum in the wall-normal direction.

5. Conclusions

In this work, the AMI equation is extended to BLs with variable density and viscosity. The resulting equation, Eq. (2.7), is part of a larger family of moment-of-momentum integral equations, the simplest being the von Kármán momentum integral equation (the zeroth moment). The AMI equation is derived using density-weighted (Favre) averaging with the streamwise momentum deficit equation. The first moment of momentum about $y = \ell$ is integrated in the wall-normal direction and normalized to phrase the AMI equation in terms of the skin-friction coefficient. Most importantly, the length scale, ℓ, about which the moment is taken must be carefully chosen such that the skin friction of an equivalent laminar boundary condition is isolated into a single term. This choice allows for the other terms in the AMI equation to be straightforwardly interpreted as enhancements (or attenuations) of skin friction relative to the laminar baseline case. For compressible BLs with variable viscosity, a reference viscosity must also be chosen. The AMI equation itself provides a strong mathematical and physical basis for choosing the gradient-weighted viscosity, μ_2, as the representative viscosity of the boundary layer.

The compressible AMI equation was applied to DNS data from turbulent BLs having a range of freestream Mach numbers, M_e, and wall temperature boundary conditions, T_w. Relative to laminar BLs with the same M_e, T_w, and momentum thickness Reynolds number based on μ_2 (Re_2) the trend in skin friction for turbulent BLs closely followed the trend in the Reynolds shear stress integral. A closer inspection of the Reynolds shear stress integrand revealed that the lower skin friction for higher M_e, higher T_w cases is associated primarily with lower near-wall mean densities.

The effect of compressibility on skin-friction coefficient may be summarized as follows. Fluid entrained into the BL from the freestream is decelerated with little pressure variation across the BL, leading to higher temperatures and lower densities in the near-wall region. Turbulent enhancement of wall shear stress relies mostly on the transport of momentum across the BL by the Reynolds shear stress, $-\overline{\rho}\widetilde{u''v''}$. Normalized by the the edge velocity, U_e^2, the covariance of streamwise and wall-normal fluctuations does not vary strongly with M_e and T_w. However, the mean density drops significantly in the near-wall region for high M_e and T_w, significantly decreasing the turbulent momentum flux, leading to lower skin-friction coefficients.

In conclusion, the AMI equation is shown to be a practical tool for using DNS (or experimental) data to elucidate essential physics in high-speed turbulent BLs. At high Mach numbers, the surface heat transfer is often of greater concern than the skin friction drag. Thus, future work will extend the concept of the AMI equation to develop a similar quantitative relationship for how the Stanton number relates to turbulent flow features throughout and above the BL. Work is already underway using perfect gas assumptions, and future plans also include extensions to include high-enthalpy effects in this type of analysis. Ultimately, this line of research can provide a stronger, more quantitative understanding of the relationship between transitional and turbulent flow physics and the dangerously high surface heat fluxes on hypersonic vehicles.

Acknowledgments

AK and PJ acknowledge helpful discussions with Kevin Griffin regarding the scaling of compressible turbulent boundary layer profiles.

REFERENCES

BANNIER, A., GARNIER, E. & SAGAUT, P. 2015 Riblet flow model based on an extended FIK identity. *Flow Turbul. Combust.* **95**, 351–376.

DI RENZO, M., FU, L. & URZAY, J. 2020 HTR solver: an open-source exascale-oriented task-based multi-GPU high-order code for hypersonic aerothermodynamics. *Comp. Phys. Commun.* **255**, 107262.

ELNAHHAS, A. & JOHNSON, P. 2022 On the enhancement of boundary layer skin friction by turbulence: an angular momentum approach. *J. Fluid Mech.* **940**, A36.

FARRELL, B.F. & IOANNOU, P.J. 2012 Dynamics of streamwise rolls and streaks in turbulent wall-bounded shear flow. J. Fluid Mech. **708**, 149–196.

FU, L., HU, X. & ADAMS, N. 2016 A family of high-order targeted ENO schemes for compressible-fluid simulations. *J. Comput. Phys.* **305**, 333–359.

FUKAGATA, K., IWAMOTO, K. & KASAGI, N. 2002 Contribution of Reynolds stress distribution to the skin friction in wall-bounded flows. *Phys. Fluids.* **14**, L73–L76.

GOTTLIEB, S., SHU, C. & TADMOR, E. 2001 Strong stability-preserving high-order time discretization Methods. *SIAM Rev.* **43**, 89–112.

KIANFAR, A., ELNAHHAS, A. & JOHNSON, P. 2022 Quantifying how turbulent fluctuations enhance skin friction and surface heat transfer in boundary layers. *AIAA Paper* 2022–094.

KIM, J. 2011 Physics and control of wall turbulence for drag reduction. *Phil. Trans. R. Soc. A.* **369**, 1396–1411.

MARUSIC, I. & MONTY, J. 2019 Attached eddy model of wall turbulence. *Annu. Rev. Fluid Mech.* **51**, 49–74.

PIROZZOLI, S. 2010 Generalized conservative approximations of split convective derivative operators. *J. Comput. Phys.* **229**, 7180–7190.

ROBINSON, S. 1991 Coherent motions in the turbulent boundary layer. *Annu. Rev. Fluid Mech.* **23**, 601–639.

SMITS, A., MCKEAN, B. & MARUSIC, I. 2011 HighReynolds number wall turbulence. *Annu. Rev. Fluid Mech.* **43**, 353–375.

WILLIAMS, C., DI RENZO, M., MOIN, P. & URZAY, J. 2021 Locally self-similar formulation for hypersonic laminar boundary layers in thermochemical nonequilibrium, *Annual Research Briefs*, Center for Turbulence Research, Stanford University, 119–128.

WU, X., MOIN, P., WALLACE, J. M., SKARDA, J., LOZANO-DURÁN, A. & HICKEY, J.-P. 2017 Transitional-turbulent spots and turbulent-turbulent spots in boundary layers, *Proc. Natl. Acad. Sci. U.S.A.* **114**, E5292–E5299.